

Temperature-Dependent Vapor Infiltration of Sulfur into Highly Porous Hierarchical Three-Dimensional Conductive Carbon Networks for Lithium Ion Battery Applications

Heather Cavers, Helge Krüger, Oleksandr Polonskyi, Fabian Schütt, Rainer Adelung,* and Sandra Hansen*



Cite This: *ACS Omega* 2020, 5, 28196–28203



Read Online

ACCESS |



Metrics & More

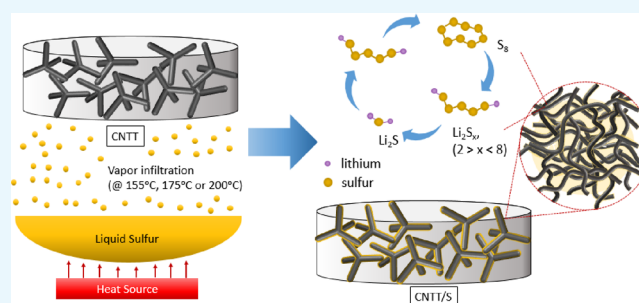


Article Recommendations



Supporting Information

ABSTRACT: Hierarchical, conductive, porous, three-dimensional (3D) carbon networks based on carbon nanotubes are used as a scaffold material for the incorporation of sulfur in the vapor phase to produce carbon nanotube tube/sulfur (CNTT/S) composites for application in lithium ion batteries (LIBs) as a cathode material. The high conductivity of the carbon nanotube-based scaffold material, in combination with vapor infiltration of sulfur, allows for improved utilization of insulating sulfur as the active material in the cathode. When sulfur is evenly distributed throughout the network via vapor infiltration, the carbon scaffold material confines the sulfur, allowing the sulfur to become electrochemically active in the context of an LIB. The electrochemical performance of the sulfur cathode was further investigated as a function of the temperature used for the vapor infiltration of sulfur into the carbon scaffolds (155, 175, and 200 °C) in order to determine the ideal infiltration temperature to maximize sulfur loading and minimize the polysulfide shuttle effect. In addition, the nature of the incorporation of sulfur at the interfaces within the 3D carbon network at the different vapor infiltration temperatures will be investigated via Raman, scanning electron microscopy/energy dispersive X-ray, and X-ray photoelectron spectroscopy. The resulting CNTT/S composites, infiltrated at each temperature, were incorporated into a half-cell using Li metal as a counter electrode and a 0.7 M LiTFSI electrolyte in ether solvents and characterized electrochemically using cyclic voltammetry measurements. The results indicate that the CNTT matrix infiltrated with sulfur at the highest temperature (200 °C) had improved incorporation of sulfur into the carbon network, the best electrochemical performance, and the highest sulfur loading, 8.4 mg/cm², compared to the CNTT matrices infiltrated at 155 and 175 °C, with sulfur loadings of 4.8 and 6.3 mg/cm², respectively.



1. INTRODUCTION

There is a growing demand for energy worldwide, and to cope with this demand, there is an increasing need for higher capacity energy storage materials that can be fabricated from cheap earth-abundant materials. Sulfur-based cathodes have a high theoretical storage capacity (over 1600 mAh/g_{sulfur}^{1–4}), for application in lithium ion batteries, based on the conversion reaction of the cyclic S₈ molecule with lithium to form smaller lithium polysulfides up to Li₂S.⁵ Two electrons per sulfur atom can be reversibly incorporated, which is 3–5 times higher than for the transition metal ions in the more conventional metal oxide cathode materials currently used in the industry.^{3,4}

Since sulfur and lithium sulfide are insulators, it is necessary to incorporate sulfur into a conductive matrix material in order to enable charge uptake in the cathode. Carbon nanotubes are an ideal candidate for this^{6–14} due to their high intrinsic carrier mobilities and current-carrying capacity. In addition, carbon nanotubes can be processed at room temperature and offer high fabrication flexibility.¹⁵

There are a variety of proposed methods for the incorporation of sulfur into conductive matrix materials including melt infiltration,^{16,17} chemical infiltration,¹⁸ and electrolysis.⁵¹ From these techniques, melt infiltration is the most efficient for maximizing the amount of sulfur, although with these techniques, the smallest pores (in the micropore range, diameter, $D < 2$ nm) remain elusive, and the utilization of sulfur is lower due to thicker insulating layers, compared to the ~1 nm sulfur layer thickness achievable through vapor infiltration.⁶ Wet chemical techniques are problematic for large-scale fabrication potential due to the toxicity of the reagents used in these processes (like carbon disulfide, CS₂, or

Received: August 17, 2020

Accepted: September 24, 2020

Published: October 19, 2020



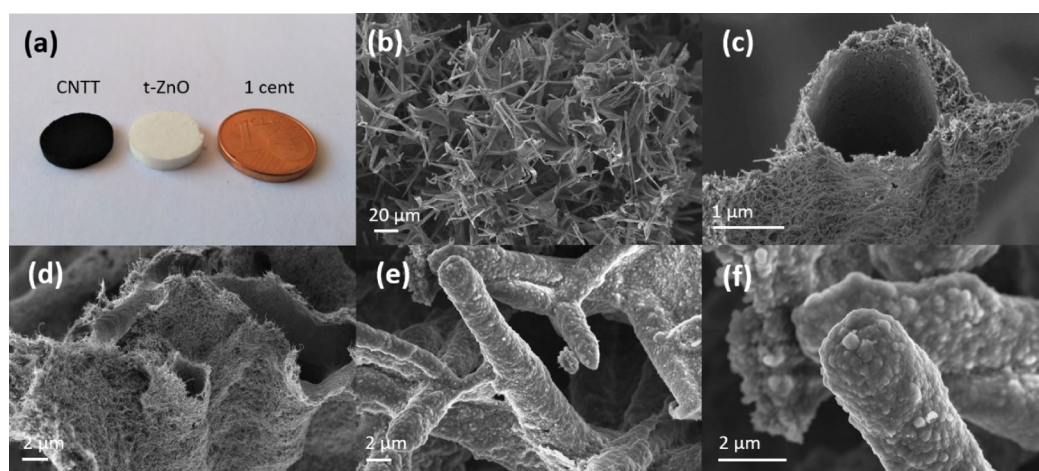


Figure 1. Scanning electron microscopy images of the CNTT/S cathode material before and after cycling. Panel (a) shows a size comparison of the CNTT and t-ZnO template used. Panels (b, c) show the CNTT sample prior to sulfur infiltration. (d) CNTT/S sample after sulfur infiltration, where the sulfur is hardly visible in SEM. (e, f) CNTT/S cathodes infiltrated at 200 °C postmortem after 10 cycles.

hydrogen sulfide, H_2S). For this reason, an alternative method reported recently in the literature is employed, namely, vapor-condensation infiltration.^{6,7}

Not only is vapor infiltration a green, solvent-free method, but it is also a scalable synthesis route for the production of sulfur–carbon composite materials for lithium sulfur batteries. This sulfur infiltration method requires relatively low temperatures (maximum 200 °C) and uses the reactants efficiently to produce very little waste and maximize the attainable capacity of the sulfur cathodes. These benefits make sulfur cathodes produced with vapor infiltration an attractive candidate to replace current industry-standard cathode materials: metal oxides. Metal oxide cathodes possess lower theoretical capacities (100–330 mAh/g) and typically require complicated production techniques, often with toxic byproducts.^{5,2} Vapor infiltration allows the sulfur to access mesopores (diameter of 2 nm < D < 50 nm) of the structure that would normally not be available in other conventional sulfur infiltration methods.^{6,19,20} In addition, the sulfur is adsorbed to the surface,⁶ resulting in thin layers of sulfur at all points in the network, maintaining their intrinsic composition and structure, optimizing the sulfur usage.

The sulfur loading of the material is mainly determined by the volume and surface area of the carbon matrix material. Recent developments in research have focused on using open porous materials to ensure accessibility of the whole host matrix, including small pore areas, for infiltration with active sulfur.^{6,7,19,20} Schütt et al. have recently developed a macroscopic, highly porous, mechanically stable carbon nanotube tube (CNTT) material based on MWCNTs and prepared using a sacrificial ZnO template.²¹ The CNTT matrix material possesses porosities of ~95%, and the open pore structure increases the accessibility of the surface area. These material properties allow for high areal sulfur loading capabilities while still maintaining direct contact between the insulating sulfur active material and the conductive carbon network at every point to maximize the sulfur utilization.

One of the major drawbacks of lithium sulfur cathode materials is the tendency of lithium polysulfides to be dissolved by the electrolyte, which causes the polysulfides to migrate away from the cathode, leading to an overall capacity loss. For this reason, it is important to understand how the sulfur is

incorporated into the carbon matrix during the vapor infiltration process in order to create a strategy to prevent the dissolution of polysulfides.

This study investigates the effect of vapor infiltration of elemental sulfur into a 3D carbon network. Using different temperatures during this procedure, the chemical interaction of the as-deposited sulfur with the surrounding carbon matrix is analyzed to understand the optimal infiltration temperature and sulfur loading in a highly porous 3D network in order to obtain a high capacity of the sulfur cathodes. The effect of infiltrating sulfur at different temperatures was investigated as different sulfur condensation behaviors have been reported at different temperatures^{6,22} in order to determine the ideal temperature for maximizing the sulfur loading and minimizing the dissolution of polysulfides during cycling.

2. RESULTS AND DISCUSSION

2.1. Characterization of the CNTT Matrix and CNTT/S Composites. The open pore structure and the even distribution of the CNTs throughout the network can be observed in the SEM images shown in Figure 1. Figure 1a demonstrates the size and shape of the sacrificial t-ZnO template and resulting CNTT sample using a coin as a reference in the image. The CNTT host matrix material prior to infiltration with sulfur is shown in Figure 1b,c. The hollow, interconnected tetrapods making up the host matrix are seen in Figure 1b. A broken tetrapod arm in Figure 1b demonstrates the thickness (<1 μm) of the entangled CNT network. In Figure 1d, after the infiltration of sulfur into the CNTT network, no sulfur aggregates are observed, suggesting an even distribution of sulfur throughout the carbon network.

In Figure 1e,f, the SEM images display the carbon nanotube sample vapor infiltrated with sulfur at 200 °C, CNTT/S@200 °C, after cycling. These images demonstrate that the hierarchical, porous, tetrapodal structure is maintained during cycling. In addition, residual electrolyte can be clearly observed coating the individual tetrapodal arms. From this, it can be concluded that at every point of the network, the electrolyte can interact with the matrix and that there is little diffusion limitation for the electrolyte. In this way, the free volume inside the matrix acts as a reservoir for the electrolyte, allowing easy access of the electrolyte to sulfur in the network and

resulting in faster uptake of Li^+ by the network. The containment of the electrolyte and any dissolved lithium polysulfides within the matrix material can also limit the polysulfide shuttle effect as the dissolved polysulfides have a higher possibility to interact with the network again than to diffuse to the counter electrode.

This homogeneous, conductive framework also possesses a hierarchical pore structure, with pores ranging from the micrometer range to the nanometer range, allowing for easy access of sulfur vapor throughout the network and a presumed confinement of sulfur in nanometer-sized pores.²⁵ The good distribution of sulfur throughout the network is demonstrated below in Figure 2.

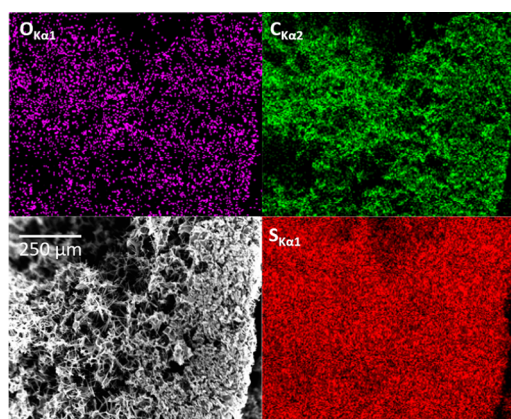


Figure 2. Qualitative cross-sectional EDX data of a CNTT/S-200 sample showing the elemental mapping of carbon, sulfur, and oxygen.

The EDX data (Figure 2) of the CNTT/S@200 °C sample demonstrates an even distribution of sulfur throughout the carbon matrix. There appears to be no sulfur gradient throughout the breadth of the CNTT matrix as the sulfur is uniformly infiltrated in the carbon matrix. The presence of oxygen in the sample can also be seen, although from the low percentage, it is most likely due to disordered carbon in the network, which can possess trace amounts of oxygen-containing impurities.³⁶ In addition, the lack of Zn observed in the sample with EDX indicates that the carbothermal reduction reaction is an effective way to remove the template material from the CNTT scaffold.

In order to further analyze the incorporation of sulfur into the carbon host matrix, X-ray photoelectron spectroscopy, a surface analysis technique, was used for investigation of the CNTT/S samples (Figure 3). The atomic percentages determined by XPS are reported below in Table 1. The relative sulfur densities of samples CNTT/S@155 °C, CNTT/S@175 °C, and CNTT/S@200 °C are also reported in Table 1, where it can be seen that the density of sulfur increases with the temperature of infiltration.

The resolved C 1s XPS data for the CNTT/S samples and the reference sample is shown below in Figure 4a, and the resolved S 2p for the CNTT/S is shown in Figure 4b.

The spectra were fitted with two carbon peaks, which are indicated with dotted lines. The peak at 284.8 eV is characteristic of C–C bonds, and the broader, low intensity peak centered at around 286 eV results from defect carbon present in the CNTT matrix material,^{26,27} most likely from trace oxygen present in the network, as seen in the EDX data in Figure 2. There is no shift in the carbon binding energy

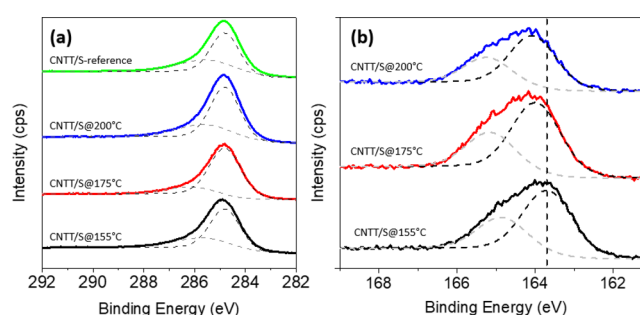


Figure 3. Resolved XPS spectra for (a) C 1s and (b) S 2p for CNTT/S @200 °C (blue), CNTT/S@175 °C (red), and CNTT/S@155 °C (black) samples; the CNTT/S-reference C 1s spectrum shown in green. S 2p_{3/2} peaks are indicated with a black dotted line, and S 2p_{1/2} peaks are indicated with a gray dotted line.

Table 1. Elemental Percentages Calculated from the Resolved XPS Spectra for CNTT/S Samples Heated to 155, 175, and 200 °C and Sulfur Areal Loading (mg/cm²) and the Total Areal Density of the CNTT/S Sample (mg/cm²) Determined by the Sample Weights before and after Sulfur Infiltration

samples	C 1s peak area (%)	O 1s peak area (%)	S 2p peak area (%)	sulfur areal loading (mg/cm ²)	total areal density (mg/cm ²)
CNTT/S@155 °C	91.6	4.0	4.4	4.8	16.8
CNTT/S@175 °C	87.4	5.4	7.2	6.3	18.2
CNTT/S@200 °C	88.8	4.4	6.8	8.4	19.7

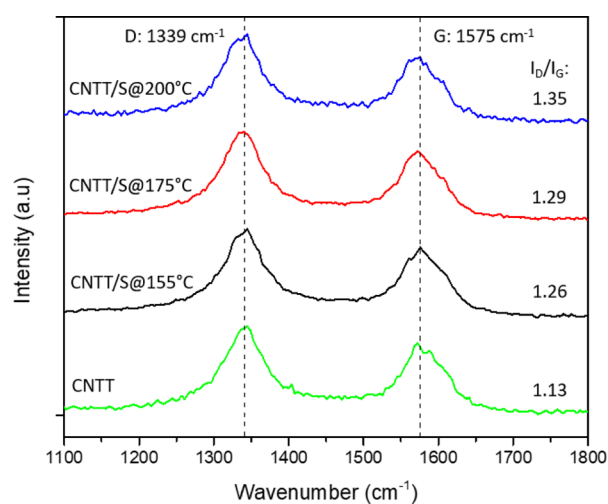


Figure 4. Raman spectra of the pristine CNTT matrix (green), sulfur-infiltrated CNTT matrix at 155 (black), 175 (red), and 200 °C (blue) measured with a laser wavelength of 532 nm.

observed for the samples sulfur infiltrated with different temperatures; however, a shift in the sulfur binding energy is apparent. The low attenuation depth of XPS (10 nm) means that only sulfur present on the surface of the carbon network is being observed. The S 2p_{3/2} and 2p_{1/2} peaks resulting from S–S binding interactions²⁸ are indicated with dotted lines in Figure 3. The lack of a S–C peak at a shift of around 163.5 eV

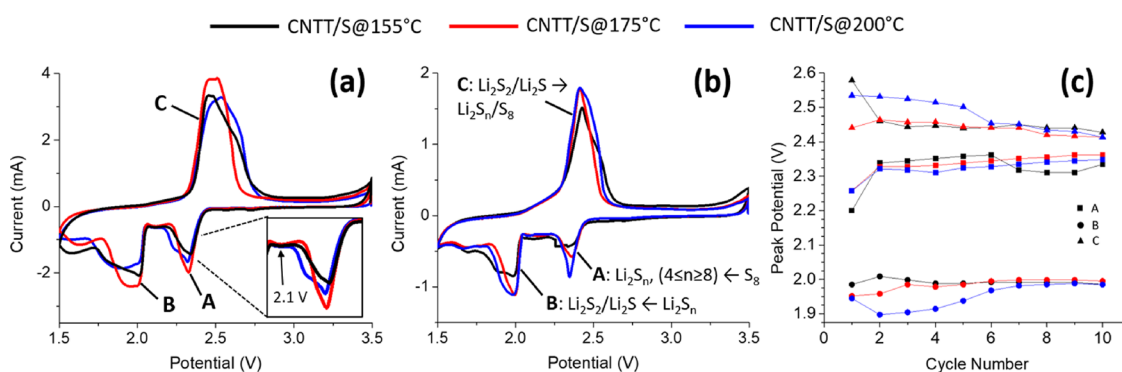


Figure 5. Representative cyclic voltammetry curves of CNTT/S cathodes prepared at 155 (black), 175 (red), and 200 °C (blue) showing current (mA) vs. potential (V) for the (a) 2nd cycle and the (b) 10th cycle. The reactions for the two reduction peaks (A and B) and the oxidation peak (C) are labeled in panel (b). The inset in Figure 6a emphasizes the change in peak with varying temperature. Panel (c) shows the trend of the individual peak positions taken from the CV curves with the cycle number. All results displayed are normalized for the amount of sulfur present in the matrix.

for S $2p_{3/2}$ ²⁹ indicates that the sulfur in the carbon matrix is merely adsorbed to the surface. The S $2p_{3/2}$ peak has the lowest binding energy, 163.7 eV, for the CNTT/S sample infiltrated at the lowest temperature (155 °C) and gradually increases with increasing infiltration temperatures. The sample infiltrated at 200 °C has the highest binding energy at 164.1 eV. The low binding energy of the CNTT/S@155 °C sample indicates that the sulfur adsorbed in the network after vapor infiltration is interacting more strongly with the carbon matrix^{28,30} than the samples infiltrated at higher temperatures. This is likely due to the low amount of sulfur in the CNTT/S@155 °C network, 4.8 mg/cm² rather than 8.4 mg/cm², as for CNTT/S@200 °C. This corresponds to overall gravimetric capacities of 477 and 712 mAh/g for the CNTT/S@155 °C and CNTT/S@200 °C samples, respectively. These gravimetric capacities, though extremely competitive compared to industry-standard cathodes,⁵² could still be improved through modification of the carbon scaffold to minimize the weight of the scaffold. The elemental percentages of sulfur on the surface of each of the samples were calculated using the peak areas from the resolved XPS spectra, and the results are displayed in Table 1. From the areal densities of sulfur and the total areal density, it can be seen that the sulfur content is much higher than the elemental percentages measured by XPS, also shown in Table 1. From this, it can be inferred that the majority of sulfur contained in the carbon network is incorporated more deeply than the top 10 nm of the sample surface.

The high sensitivity of Raman spectroscopy to changes in the structure of the carbon matrix material makes it ideal to investigate the CNTT material before and after the incorporation of sulfur into the network in order to determine the impact the adsorbed sulfur has on the structure. The resulting Raman spectra are shown below in Figure 4. No characteristic peaks of elemental sulfur below 500 cm⁻¹ were detected.¹ The lack of sulfur peaks in the spectra also indicates that the sulfur is well dispersed in the network, as seen in the EDX data (Figure 2), without long-range ordering,³¹ possessing strong absorption and interaction with the carbon matrix material.³²

The main peaks observed in the CNTT reference and CNTT/S samples (Figure 4) were located at 1339 and 1575 cm⁻¹ belonging to the D and G bands of carbon, respectively. The G band originates from the in-plane vibrations of sp² carbon atoms contained in the hexagonal bonding structure of

the MWCNTs, and the D band originates from defects in the carbon matrix.³³ Since no sulfur peaks could be measured directly for these samples, the intensities of the corresponding D and G bands are further investigated. The ratio of the intensities of the D and G bands, I_D/I_G , can be used in comparing the degree of crystallinity of carbon networks.^{32–34} The intensity of the defect sp³ hybridized carbon peak (D) increases significantly, and the in-plane sp² carbon (G) decreases with increasing sulfur content. This corresponds to an increase in the I_D/I_G ratio (from 1.13 (CNTT) to 1.35 (CNTT/S@200 °C)), which indicates the presence of more lattice defects³⁴ for samples that sulfur infiltrated at higher temperatures and corresponds to more sulfur present in the network.³⁵ From the XPS analysis, it was seen that for sample CNTT/S@200 °C, the majority of sulfur was incorporated into pores in the network. The high I_D/I_G ratio for CNTT/S@200 °C supports the incorporation of sulfur into defect sites or pores in the carbon network³² rather than on the surface.

From Table 1, the relative percentage of sulfur on the surface of CNTT/S@200 °C determined by XPS is lower than that of sample CNTT/S@175 °C, though the overall sulfur loading was higher. It is implied that the majority of sulfur is incorporated in the pores in the CNTT network, which would not be observable in a surface analysis, such as XPS. This is most pronounced for the CNTT/S@200 °C sample. This may be explained by the different sulfur conformations present in the vapor phase. At temperatures of 200 °C, the sulfur vapor possesses a fraction of S₆.³⁶ These smaller molecules can be more easily incorporated into the defect sites of the carbon network, which in turn could result in a preferential incorporation of sulfur into smaller pores formed by the entangled CNT network (<10 nm)^{37,38} compared to samples infiltrated at lower temperatures. The incorporation of sulfur into small pores in carbon networks has been shown to improve the capacity retention of sulfur^{8,19,39,40} as further demonstrated during the cyclic voltammetry measurements of CNTT/S@200 °C as a cathode in an LIB half-cell.

2.2. Electrochemical Characterization. In the following, the results of the cyclic voltammetry measurements are discussed for the CNTT/S samples prepared with varying sulfur infiltration temperatures. The electrolyte contained 0.7 M LiTFSI in DME/DOL (2:3, v/v) with 0.25 M LiNO₃ added to promote passivation on the surface of the Li-metal counter electrode.¹ Based on the discussion of the sulfur and carbon

interactions in Section 2.1, it is investigated here how these findings influence the battery performance of the CNTT/S composites (Figure 5).

Two reduction peaks and a broad oxidation peak are clearly visible in the CV curves in the 2nd cycle (Figure 5a) and the 10th cycle (Figure 5b). Figure 5a shows the second cycle for the CNTT/S samples infiltrated at different temperatures. The second cycle for the CNTT/S@155 °C sample is shown in black, the CNTT/S@175 °C sample is shown in red, and the CNTT/S@200 °C sample is shown in blue. The same color coding was used to display the resulting CV curves for the 10th cycle (Figure 5b) and the relationship of the peak potentials to the cycle number (Figure 5c). The two cathodic reduction peaks appearing between 2.3–2.4 V (A) and 1.9–2.0 V (B), labeled in Figure 5b, result from the reduction of S_8 to long chain polysulfides (Li_2S_n , $4 \leq n \leq 8$) and the reduction of long chain polysulfides to insoluble Li_2S_2/Li_2S species, respectively.⁴¹ The first reduction peak, A, is most likely associated with the formation of Li_2S_4 compounds as the S_4^{2-} species is the most stable reaction intermediate in DOL/DME solvents and other low donor solvents.⁴² The broad anodic peak centered around 2.45 V (labeled as C in Figure 5b) corresponds to the oxidation of the short- and long-chain lithium sulfides to S_8 . Since the oxidation peak is rather broad, it is likely that different peaks are overlapping due to the fact that many polysulfides coexist and appear at similar potential values.⁴⁹ In addition, the width of the second cathodic peak, B, occurring in the CV curves for all samples between 1.9 and 2.0 V, is likely due to an overlap of multiple reduction reactions.⁴⁶ In Figure 5a, in all the CV curves, there is a low intensity peak around 2.1 V (shown in the Figure 5a inset), which disappears after repeated cycling. This peak is likely due to an intermediate species that possesses low stability produced during the first redox processes.⁴³ Due to the instability of this intermediate species, it is usually only detectable at low scan rates and for cathode samples possessing a highly conductive matrix with good charge transfer capabilities.⁴⁹ A broad peak around 1.7 V is present, which is lower than the expected reduction reaction to produce Li_2S_2 . This peak is likely attributed to the decomposition reaction of $LiNO_3$ at the cathode,⁸ which likely contributes to the low Coulombic efficiencies shown in supplemental Figure S1.

The voltages corresponding to the reduction and oxidation peaks from the CV curves that were plotted against the cycle number and the trends in the peak position (V) of the reduction peaks and oxidation peak with the cycle number can be seen in Figure 5c. Peak A, which corresponds to the first reduction reaction of the long-chain polysulfides, is seen to experience a gradual potential increase for all samples with ongoing cycling. The shift to higher potentials indicates that better redox reversibility for this reaction is obtained in later cycles.⁴⁴ From the first to the second cycle, the second reduction peak, B, for sample CNTT/S@200 °C (blue) shifts to lower peak potentials, most likely due to side reactions or SEI formation that can lead to an initial polarization⁴⁵ and then begins to shift to higher potentials and stabilizes after six cycles. For samples CNTT/S@175 °C (red) and 155 °C (black), the potentials remain relatively stable. Peak C represents the oxidation reactions and for all samples that experience a continuous decrease in peak potential over all cycles. There is a similar trend with the potentials of peak C as with peak B, where the potential stabilizes after six cycles.

In the second cycle, sample CNTT/S@155 °C (black) has the largest difference in peak potential between the reduction and oxidation peaks, indicating a higher degree of polarization,^{9,41,45} likely due to the lower affinity of the sulfur to the host matrix^{44,47} and more sluggish reaction kinetics.⁴⁸ Whereas, sample CNTT/S@175 °C (red) has the smallest difference in peak potential in the initial cycles, and the CV curves possess sharper and narrower peaks from the first cycles on, indicating better reaction kinetics and a lower degree of polarization⁵⁰ from the beginning than the other two samples.

From the peak trends in Figure 5c, it can be seen that for sample CNTT/S@200 °C (blue), the peak potentials for both the reduction and oxidation peaks begin to stabilize after six cycles. After which, the peak potentials were at slightly lower voltages (for the oxidation peaks) and slightly higher voltages (for the reduction peaks). This indicates improved reaction kinetics in the later cycles⁴⁸ and a higher affinity for the host matrix. From the reduction curve areas shown in the Supporting Information, page S2, it can be seen that the sample CNTT/S@200 °C experiences the smallest change in the total curve area over 10 cycles. This is likely due to the presence of more defect sites in sample CNTT/S@200 °C, seen in Figure 4, and the preferential incorporation of sulfur into the defect sites and the accessibility of smaller pores in the carbon matrix material for sulfur vapor at higher temperatures¹⁸ as discussed in the previous section. All three samples retain similar peak shapes to the second cycle, Figure 5a, which demonstrates good reversibility and stability of the electrochemical reactions. In the inset in Figure 5a, it can be seen that for reduction peak A, there is a shoulder present for sample CNTT/S@200 °C likely because of better resolution of the different reduction reactions occurring, which could be due to a more efficient interaction between the sulfur and the conductive carbon scaffold. In addition, in Figure 5b, it can be seen that for sample CNTT/S@200 °C, the first reduction peak, A, is considerably sharper after 10 cycles than the samples infiltrated at lower temperatures, indicating that the sulfur is better confined in the network, and the dissolution of the long-chain polysulfides is reduced. This suggests that the incorporation of sulfur into the defect sites in the carbon matrix at a higher temperature, especially 200 °C, serves to stabilize the polysulfides and reduce their dissolution into the electrolyte.

3. CONCLUSIONS

Conductive 3D carbon nanotube networks were successfully used as a scaffold material to accommodate sulfur for the preparation of sulfur cathodes for lithium ion battery applications. Vapor infiltration of sulfur into the carbon matrix material led to even distribution of sulfur throughout the networks, improving the utilization of the active material in the cathode during cycling. The preferential incorporation of sulfur into the defect sites in the network was observed with Raman spectroscopy, an effect that became more pronounced with the highest infiltration temperature, 200 °C. The improved incorporation of sulfur into the network for the sample infiltrated at the highest temperature (CNTT/S@200 °C) resulted in the best capacity retention and overall sulfur usage for longer cycling. However, marginally superior reaction kinetics were found with the cathode sample vapor infiltrated at 175 °C, implying that a balance is required between the sulfur–carbon interaction and incorporation of the sulfur in the smaller pores in the matrix. At the lowest temperature, 155

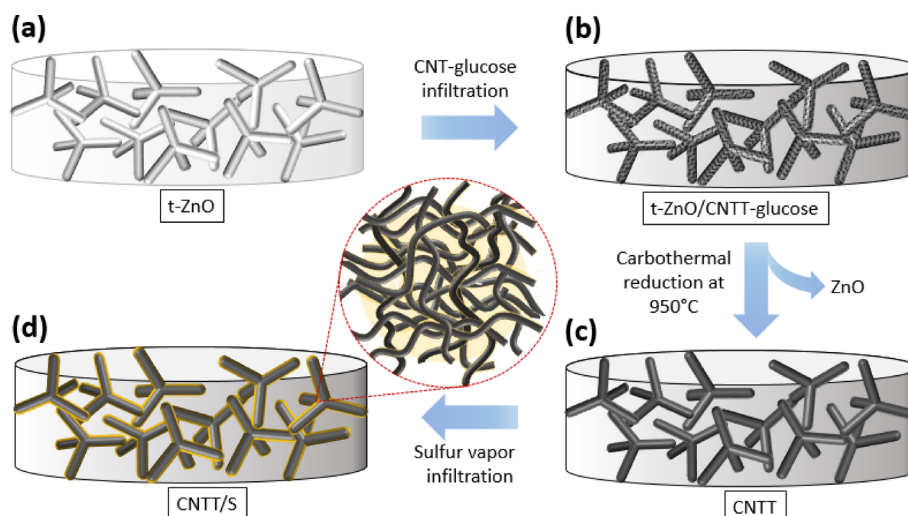


Figure 6. Schematic illustration of the preparation process used for the CNTT/S samples, where panel (a) is the sacrificial t-ZnO template, panel (b) is the t-ZnO infiltrated with an aqueous CNT–glucose solution (steps as described by Schütt et al.²¹), panel (c) is the hollow tetrapodal CNT matrix after carbothermal reduction and ZnO removal, and panel (d) is the CNTT matrix after vapor infiltration with sulfur to form CNTT/S cathodes. The inset in panel (d) shows sulfur incorporation into the self-entangled CNT network making up the CNTT scaffold.

°C, the sulfur is not as efficiently incorporated into the pores in the network and is thus more accessible to the electrolyte, and the CNTT/S cathodes are subject to increased capacity fading and greater polarization effects. Repeated cycling of the CNTT/S cathode samples led to a shift in the voltage for the polysulfide oxidation reactions to lower voltages and polysulfide reduction reactions to higher voltages, indicating improvement of the potentiostatic cycling and redox reaction reversibility. The use of 3D carbon matrix materials with hierarchical pore structures can lead to improved areal sulfur loading, active sulfur utilization, and better overall reaction kinetics.

4. MATERIAL AND METHODS

4.1. Fabrication of the 3D CNTT Matrix Material and Subsequent CNTT/S Composite Fabrication. Tetrapodal zinc oxide (t-ZnO) was used as a sacrificial template in order to prepare highly porous 3D carbon nanotube tube (CNTT) networks as demonstrated in the schematic illustration in Figure 6.

Tetrapodal zinc oxide (t-ZnO) networks used for the preparation of the conductive carbon matrix material were produced by a simple flame transport synthesis as described by Mishra et al.²³ The t-ZnO powder was pressed into cylinders with a height of 2 mm and diameter of 12 mm, possessing densities of 0.36 g/cm³, and sintered at 1150 °C for 5 h to form an interconnected network of t-ZnO, Figure 6a, as described by Schütt et al.²¹ An aqueous 1 wt % solution of MWCNTs (CarboByk 9310 from BYK-Chemie) was prepared with an addition of 10 wt % glucose for the following carbothermal reduction reaction and treated to ultrasonication for 5 min prior to infiltration into the t-ZnO template to ensure a well-mixed dispersion. The aqueous solution was infiltrated into the t-ZnO templates on a hot plate at 50 °C and allowed to dry to form t-ZnO/CNTT–glucose templates (Figure 6b). A carbothermal reduction reaction²⁴ was used to remove the sacrificial t-ZnO by heating the t-ZnO/CNTT–glucose composites in a quartz tube under an inert Ar gas atmosphere at 950 °C for 5 h. The resulting CNTT matrices

possessed porosities of about 95% and densities of 0.06 g/cm³ (Figure 6c).

The vapor infiltration of sulfur into the CNTT matrix materials, to produce carbon nanotube tube/sulfur (CNTT/S) composites, was performed using a round bottom flask. A sufficient amount of powdered sulfur, 1–2 g based on the weight of the carbon matrix material, was added to the bottom of the flask. A stainless steel mesh was inserted to suspend the CNTT matrix material 1–2 mm above the sulfur reservoir. The flask was sealed with the CNTT samples inside the glove box under an argon atmosphere in order to prevent any oxidation during the sulfur infiltration process. The flask containing the CNTT samples was then heated in an oil bath for 2 h at 155, 175, and 200 °C for samples CNTT/S@155 °C, CNTT/S@175 °C, and CNTT/S@200 °C, respectively (Figure 6d). The temperature of the oil bath and the inside of the flask was monitored, and the temperatures reported reflect the temperature of the flask. All samples were weighed before and after vapor infiltration in order to determine the resulting sulfur weight percent.

4.2. Chemical and Electrochemical Investigation of CNTT/S Composites. The CNTT/S samples were analyzed prior to electrochemical analysis with Raman spectroscopy, scanning electron microscopy, energy dispersive spectroscopy, and X-ray photoelectron spectroscopy in order to determine how well the sulfur infiltrated into the matrix material. All Raman spectroscopy analysis was done using an alpha 300 RA, WITech system, with a CCD detector and triple-grating spectrometer of 600 gr/mm at an excitation wavelength of 532.2 nm. Scanning electron microscopy (SEM) and energy dispersive X-ray spectroscopy (EDX) analysis were performed using a Zeiss Gemini Ultra55 Plus scanning electron microscope. X-ray photoelectron spectroscopy (XPS, Omicron Nano-Technology, GmbH) was performed with an Al-anode source (240 W). All spectra were referenced to aliphatic carbon at 298.4 eV, and analysis was performed with CasaXPS software.

Half-cells were prepared using a lithium foil counter electrode, three 1.5 μm glass fiber separators, and 500 μL of a 0.7 M lithium bis(trifluoromethanesulfonyl)imide, LiTFSI,

electrolyte solution in 3:2 1,3-dioxolane:1,2-dimethoxy ethane (v/v) with 0.25 M lithium nitrate, LiNO₃, added. All chemicals used in the preparation of the electrolyte were obtained from Sigma Aldrich. Cyclic voltammetry was performed on the half cells using a scan rate of 0.056 mV/s over a range of 1.5–3.5 V.

4.3. Postmortem Analysis. Analysis of the cycled cathode materials was performed *ex situ* with Raman spectroscopy. The cycled samples were sealed under an argon atmosphere in transparent polyethylene pouch cells to ensure no oxidation of the sample occurred during measurement. All Raman analysis was done using the same alpha 300 RA, WITech system as described in Section 2.2, using low power to ensure no reaction with the pouch cell or components on the sample surface.

Postmortem SEM analysis was performed using a Zeiss Gemini Ultra55 Plus scanning electron microscope with an in-lens detector. An acceleration voltage of 1–2 kV and a working distance of 1–2 mm were used.

■ ASSOCIATED CONTENT

SI Supporting Information

The Supporting Information is available free of charge at <https://pubs.acs.org/doi/10.1021/acsomega.0c03956>.

Curve areas calculated from the cyclic voltammetry measurements for the reduction steps and oxidation steps for all three samples (CNTT/S@155 °C, CNTT/S@175 °C, and CNTT/S@200 °C) plotted against the cycle number (PDF)

■ AUTHOR INFORMATION

Corresponding Authors

Rainer Adelung – University of Kiel, Institute for Material Science, 24143 Kiel, Germany; Email: ra@tf.uni-kiel.de

Sandra Hansen – University of Kiel, Institute for Material Science, 24143 Kiel, Germany; orcid.org/0000-0002-3529-8367; Email: sn@tf.uni-kiel.de

Authors

Heather Cavers – University of Kiel, Institute for Material Science, 24143 Kiel, Germany

Helge Krüger – University of Kiel, Institute for Material Science, 24143 Kiel, Germany; orcid.org/0000-0002-9638-8753

Oleksandr Polonskyi – University of Kiel, Institute for Material Science, 24143 Kiel, Germany

Fabian Schütt – University of Kiel, Institute for Material Science, 24143 Kiel, Germany

Complete contact information is available at:

<https://pubs.acs.org/doi/10.1021/acsomega.0c03956>

Notes

The authors declare no competing financial interest.

■ ACKNOWLEDGMENTS

This work was carried out in the framework of the German project “Entwicklung und Charakterisierung von großflächigen, porösen Si-Film Anoden für Lithium-Schwefel-Silizium-Energiespeichern” (PorSSi, 03XP0126 B) and partially funded by the “Federal Ministry of Education and Research” (BMBF). Special thanks goes to the EKSH for funding this project partially through the project “3D strukturierte Kohlenstoff-Schwefel Gerüstmaterialien als neuartiges und nachhaltiges Kathodenmaterial für Hochenergie Lithium-Ionen Akkus”. We acknowledge funding by the Deutsche Forschungsgemein-

schaft (DFG) under contract AD183/27-1. We further acknowledge financial support by Schleswig-Holstein within the funding programme “Open Access Publikationsfonds”.

■ REFERENCES

- (1) Hagen, M.; Hanselmann, D.; Ahlbrecht, K.; Maça, R.; Gerber, D.; Tübke, J. Lithium–Sulfur Cells: The Gap between the State-of-the-Art and the Requirements for High Energy Battery Cells. *Adv. Energy Mater.* **2015**, *5*, 1–11.
- (2) Seh, Z. W.; Sun, Y.; Zhang, Q.; Cui, Y. Designing high-energy lithium–sulfur batteries. *Chem. Soc. Rev.* **2016**, *45*, 5605–5634.
- (3) Tan, J.; Liu, D.; Xu, X.; Mai, L. In situ/operando characterization techniques for rechargeable lithium–sulfur batteries: a review. *Nanoscale* **2017**, *9*, 19001–19016.
- (4) Manthiram, A.; Fu, Y.; Chung, S. H.; Zu, C.; Su, Y. S. Rechargeable Lithium–Sulfur Batteries. *Chem. Rev.* **2014**, *114*, 11751–11787.
- (5) Hagen, M.; Schiffels, P.; Hammer, M.; Dörfler, S.; Tübke, J.; Hoffmann, M. J.; Althues, H.; Kaskel, S. In-Situ Raman Investigation of Polysulfide Formation in Li-S Cells. *J. Electrochem. Soc.* **2013**, *160*, A1205–A1214.
- (6) Carter, R.; Oakes, L.; Muralidharan, N.; Pint, C. L. Isothermal Sulfur Condensation into Carbon Scaffolds: Improved Loading, Performance, and Scalability for Lithium–Sulfur Battery Cathodes. *J. Phys. Chem. C* **2017**, *121*, 7718–7727.
- (7) Li, M.; Carter, R.; Douglas, A.; Oakes, L.; Pint, C. L. Sulfur Vapor-Infiltrated 3D Carbon Nanotube Foam for Binder-Free High Areal Capacity Lithium–Sulfur Battery Composite Cathodes. *ACS Nano* **2017**, *11*, 4877–4884.
- (8) Guo, Z.; Zhang, B.; Li, D.; Zhao, T.; Coxon, P. R.; Harris, C. J.; Hao, R.; Liu, Y.; Xi, K.; Li, X. Mixed Microporous/Low-range Mesoporous Composite with High Sulfur Loading from Hierarchically-structured Carbon for Lithium Sulfur Batteries. *Electrochim. Acta* **2017**, *230*, 181–188.
- (9) Walle, M. D.; Zhang, Z.; Zhang, M.; You, X.; Li, Y.; Liu, Y. N. Hierarchical 3D nitrogen and phosphorous codoped graphene/carbon nanotubes–sulfur composite with synergistic effect for high performance of lithium–sulfur batteries. *J. Mater. Sci.* **2018**, *53*, 2685–2696.
- (10) Sun, L.; Li, H.; Zhao, M.; Wang, G. High-performance lithium–sulfur batteries based on self-supporting graphene/carbon nanotube foam@sulfur composite cathode and quasi-solid-state polymer electrolyte. *Chem. Eng.* **2018**, *332*, 8–15.
- (11) Huang, J. Q.; Zhang, Q.; Zhang, S. M.; Liu, X. F.; Zhu, W.; Qian, W. Z.; Wei, F. Aligned sulfur-coated carbon nanotubes with a polyethylene glycol barrier at one end for use as a high efficiency sulfur cathode. *Carbon* **2013**, *58*, 99–106.
- (12) Cheng, X. B.; Huang, J. Q.; Zhang, Q.; Peng, H. J.; Zhao, M. Q.; Wei, F. Aligned carbon nanotube/sulfur composite cathodes with high sulfur content for lithium–sulfur batteries. *Nano Energy* **2014**, *4*, 65–72.
- (13) Yuan, L.; Qiu, X.; Chen, L.; Zhu, W. New insight into the discharge process of sulfur cathode by electrochemical impedance spectroscopy. *J. Power Sources* **2009**, *189*, 127–132.
- (14) Zhu, L.; Zhu, W.; Cheng, X. B.; Huang, J. Q.; Peng, H. J.; Yang, S. H.; Zhang, Q. Cathode materials based on carbon nanotubes for high-energy-density lithium–sulfur batteries. *Carbon* **2014**, *75*, 161–168.
- (15) Bryning, M. B.; Milnie, D. E.; Islam, M. F.; Hough, L. A.; Kikkawa, J. M.; Yodh, A. G. Carbon Nanotube Aerogels. *Adv. Mater.* **2007**, *19*, 661–664.
- (16) Ji, X.; Lee, K. T.; Nazar, L. F. A highly ordered nanostructured carbon–sulfur cathode for lithium–sulfur batteries. *Nat. Mater.* **2009**, *8*, 500–506.
- (17) Carter, R.; EJORH, D.; Share, K.; Cohn, A. P.; Douglas, A.; Muralidharan, N.; Tovar, T. M.; Pint, C. L. Surface oxidized mesoporous carbons derived from porous silicon as dual polysulfide confinement and anchoring cathodes in lithium sulfur batteries. *J. Power Sources* **2016**, *330*, 70–77.

- (18) Guo, J.; Xu, Y.; Wang, C. Sulfur-Impregnated Disordered Carbon Nanotubes Cathode for Lithium–Sulfur Batteries. *Nano Lett.* **2011**, *11*, 4288–4294.
- (19) Zhao, Z.; Qin, D.; Wang, S.; Chen, G.; Li, Z. Fabrication of High Conductive S/C Cathode by Sulfur Infiltration into Hierarchical Porous Carbon/Carbon Fiber Weave-Structured Materials via Vapor-Melting Method. *Electrochim. Acta* **2014**, *127*, 123–131.
- (20) Geng, X.; Yi, R.; Yu, Z.; Zhao, C.; Li, Y.; Wei, Q.; Liu, C.; Zhao, Y.; Lu, B.; Yang, L. Isothermal sulfur condensation into carbon nanotube/nitrogen-doped graphene composite for high performance lithium–sulfur batteries. *J. Mater. Sci.: Mater. Electron.* **2018**, *29*, 10071–10081.
- (21) Schutt, F.; Signetti, S.; Kruger, H.; Roder, S.; Smazna, D.; Kaps, S.; Gorb, S. N.; Mishra, Y. K.; Pugno, N. M.; Adelung, R. Hierarchical self-entangled carbon nanotube tube networks. *Nat. Commun.* **2017**, *8*, 1–10.
- (22) Steudel, R.; Steudel, Y.; Wong, M. W. *Elemental Sulfur and Sulfur Rich Compounds II*, Topics in Current Chemistry, Vol. 231, Steudel, R., Ed.; Springer-Verlag: Berlin, 2003; pp. 117–134.
- (23) Mishra, Y. K.; Kaps, S.; Schuchardt, A.; Paulowicz, I.; Jin, X.; Gedamu, D.; Freitag, S.; Claus, M.; Wille, S.; Kovalev, A.; Gorb, S. N.; Adelung, R. Fabrication of Macroscopically Flexible and Highly Porous 3D Semiconductor Networks from Interpenetrating Nanostructures by a Simple Flame Transport Approach. *Part. Part. Syst. Charact.* **2013**, *30*, 775–783.
- (24) Strubel, P.; Thieme, S.; Biemelt, T.; Helmer, A.; Oschatz, A.; Brückner, J.; Althues, H.; Kaskel, S. ZnO Hard Templating for Synthesis of Hierarchical Porous Carbons with Tailored Porosity and High Performance in Lithium–Sulfur Battery. *Adv. Funct. Mater.* **2015**, *25*, 287–297.
- (25) Carter, R.; Davis, B.; Oakes, L.; Maschmann, M. R.; Pint, C. L. A high areal capacity lithium–sulfur battery cathode prepared by site-selective vapor infiltration of hierarchical carbon nanotube arrays. *Nanoscale* **2017**, *9*, 15018–15026.
- (26) Ponraj, R.; Kannan, A. G.; Ahn, J. H.; Lee, J. H.; Kang, J.; Han, B.; Kim, D. W. Effective Trapping of Lithium Polysulfides Using a Functionalized Carbon Nanotube-Coated Separator for Lithium–Sulfur Cells with Enhanced Cycling Stability. *ACS Appl. Mater. Interfaces* **2017**, *9*, 38445–38454.
- (27) Huang, J. Q.; Xu, Z. L.; Abouali, S.; Garakani, M. A.; Kim, J. K. Porous graphene oxide/carbon nanotube hybrid films as interlayer for lithium–sulfur batteries. *Carbon* **2016**, *99*, 624–632.
- (28) Zhang, L.; Huang, H.; Xia, Y.; Liang, C.; Zhang, W.; Luo, J.; Gan, Y.; Zhang, J.; Tao, X.; Fan, H. J. High-content of sulfur uniformly embedded in mesoporous carbon: a new electrodeposition synthesis and an outstanding lithium–sulfur battery cathode. *J. Mater. Chem. A* **2017**, *5*, 5905–5911.
- (29) Bhargava, A.; Chang, C. H.; Fu, Y.; Manthiram, A. Rationally Designed High-Sulfur-Content Polymeric Cathode Material for Lithium–Sulfur Batteries. *ACS Appl. Mater. Interfaces* **2019**, *11*, 6136–6142.
- (30) Chen, X.; Xu, X.; Yang, Z.; Liu, Z.; Zhang, L.; Xu, X.; Chen, Y.; Huang, S. Sulfur-doped porous reduced graphene oxide hollow nanosphere frameworks as metal-free electrocatalysts for oxygen reduction reaction and as supercapacitor electrode materials. *Nanoscale* **2014**, *6*, 13740–13747.
- (31) Li, L.; Zhou, G.; Yin, L.; Koratkar, N.; Li, F.; Cheng, H. M. Stabilizing sulfur cathodes using nitrogen-doped graphene as a chemical immobilizer for LiS batteries. *Carbon* **2016**, *108*, 120–126.
- (32) Helen, M.; Diemant, T.; Schindler, S.; Behm, R. J.; Danzer, M.; Kaiser, U.; Fichtner, M.; Anji Reddy, M. Insight into Sulfur Confined in Ultramicroporous Carbon. *ACS Omega* **2018**, *8*, 11290–11299.
- (33) Tao, X.; Chen, X.; Xia, Y.; Huang, H.; Gan, Y.; Wu, R.; Chen, F.; Zhang, W. Highly mesoporous carbon foams synthesized by a facile, cost-effective and template-free Pechini method for advanced lithium–sulfur batteries. *J. Mater. Chem. A* **2013**, *1*, 3295–3301.
- (34) Chen, R.; Zhao, T.; Lu, J.; Wu, F.; Li, L.; Chen, J.; Tan, G.; Ye, Y.; Amine, K. Graphene-Based Three-Dimensional Hierarchical Sandwich-type Architecture for High-Performance Li/S Batteries. *Nano Lett.* **2013**, *10*, 4642–4649.
- (35) Chen, L.; Cui, X.; Wang, Y.; Wang, M.; Qiu, R.; Shu, Z.; Zhang, L.; Hua, Z.; Cui, F.; Wei, C. J.; Shi. One-step synthesis of sulfur doped graphene foam for oxygen reduction reactions. *Dalton Trans.* **2014**, *43*, 3420.
- (36) *The Sulfur Data Book*, Tuller, W. N., Ed.; McGraw-Hill Book Company Inc.: New York, 1954.
- (37) Wang, C.; Xie, B.; Liu, Y.; Xu, Z. Mechanotunable Microstructures of Carbon Nanotube Networks. *ACS Macro Lett.* **2012**, *1*, 1176–1179.
- (38) Xie, B.; Liu, Y.; Ding, Y.; Zheng, Q.; Xu, Z. Mechanics of carbon nanotube networks: microstructural evolution and optimal design. *Soft Matter* **2011**, *7*, 10039–10047.
- (39) Ye, X.; Ma, J.; Hu, Y. S.; Wei, H.; Ye, F. MWCNT porous microspheres with an efficient 3D conductive network for high performance lithium–sulfur batteries. *J. Mater. Chem. A* **2016**, *4*, 775–780.
- (40) Chen, W.; Zhang, Z.; Li, Q.; Lai, Y.; Li, J. Freestanding Sulfur/3D Carbon Fiber Membrane Cathodes for Advanced Lithium–Sulfur Batteries. *ChemElectroChem* **2015**, *2*, 246–252.
- (41) Wang, Y.; Zhang, Z.; Haibara, M.; Sun, D.; Ma, X.; Jin, Y.; Munakata, H.; Kanamura, K. Reduced Polysulfide Shuttle Effect by Using Polyimide Separators with Ionic Liquid-based Electrolytes in Lithium–Sulfur Battery. *Electrochim. Acta* **2017**, *255*, 109–117.
- (42) Zou, Q.; Lu, Y. C. Solvent-Dictated Lithium Sulfur Redox Reactions: An Operando UV–vis Spectroscopic Study. *J. Phys. Chem. Lett.* **2016**, *7*, 1518–1525.
- (43) Barchasz, C.; Molton, F.; Duboc, C.; Lepretre, J. C.; Patoux, S.; Alloin, F. Lithium/Sulfur Cell Discharge Mechanism: An Original Approach for Intermediate Species Identification. *Anal. Chem.* **2012**, *84*, 3973–3980.
- (44) Lu, H.; Wang, J.; Li, T.; Du, H.; Yi, D.; Fang, J.; Hong, B. Improved performance of lithium–sulfur battery by a functional separator design. *J. Solid State Electr.* **2018**, *22*, 953–958.
- (45) Zhang, Y.; Zhao, Y.; Bakenov, Z.; Tuiyebayeva, M.; Konarov, A.; Chen, P. Synthesis of Hierarchical Porous Sulfur/Polypyrrole/Multiwalled Carbon Nanotube Composite Cathode for Lithium Batteries. *Electrochim. Acta* **2014**, *143*, 49–55.
- (46) Wu, H. L.; Huff, L. A.; Gewirth, A. A. In Situ Raman Spectroscopy of Sulfur Speciation in Lithium–Sulfur Batteries. *ACS Appl. Mater. Interfaces* **2015**, *7*, 1709–1719.
- (47) Manan, N. S. A.; Aldous, L.; Alias, Y.; Murray, P.; Yellowless, L. J.; Llagunas, M. C.; Hardacre, C. Electrochemistry of Sulfur and Polysulfides in Ionic Liquids. *J. Phys. Chem. B.* **2011**, *115*, 13873–13879.
- (48) Zhu, P.; Zang, J.; Zhu, J.; Lu, Y.; Chen, C.; Jiang, M.; Yan, C.; Dirican, M.; Sellvan, R. K.; Kim, D.; Zhang, X. Effect of reduced graphene oxide reduction degree on the performance of polysulfide rejection in lithium–sulfur batteries. *Carbon* **2018**, *126*, 594–600.
- (49) Hou, T. Z.; Xu, W. T.; Chen, X.; Peng, H. J.; Huang, J. Q.; Zhang, Q. Lithium Bond Chemistry in Lithium–Sulfur Batteries. *Angew. Chem., Int. Ed.* **2017**, *56*, 8178–8182.
- (50) Wu, F.; Zhao, S.; Li, J.; Lu, Y.; Su, Y.; Chen, L.; Bao, L.; Yao, J.; Lin, X. Hand-in-Hand Reinforced rGO Film Used as an Auxiliary Functional Layer for High-Performance Li-S Batteries. *ACS Appl. Mater. Interfaces* **2019**, *11*, 12544–12553.
- (51) He, B.; Li, W. C.; Yang, C.; Wang, S. Q.; Lu, A. H. Incorporating Sulfur Inside the Pores of Carbons for Advanced Lithium–Sulfur Batteries: An Electrolysis Approach. *ACS Nano* **2016**, *10*, 1633–1639.
- (52) Mohamed, N.; Allam, N. K. Recent advances in the design of cathode materials for Li-ion batteries. *RSC Adv.* **2020**, *10*, 21662–21685.